Infrared Nanospectroscopy at the Graphene-Electrolyte Interface

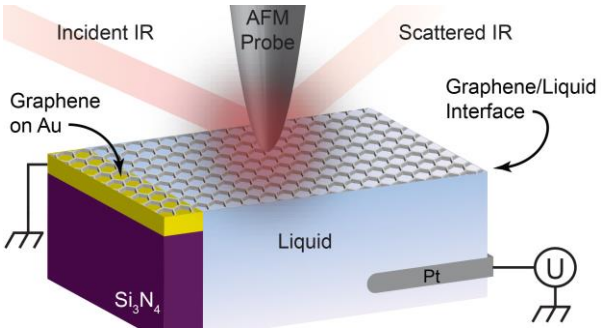

Yi-Hsien Lu [†,^], *Jonathan M. Larson* [‡,^], *Artem Baskin*[§], *Xiao Zhao*[†], *Paul D. Ashby*[§], *David Prendergast*[§], *Hans A. Bechtel*[⊥,*], *Robert Kostecki*[‡,*], *and Miquel Salmeron* [†,∥,*]

[†] Materials Sciences Division, Lawrence Berkeley National Laboratory, Berkeley, California, 94720, United States

[‡] Energy Storage & Distributed Resources Division, Lawrence Berkeley National Laboratory, Berkeley, California, 94720, United States

[§] Molecular Foundry, Lawrence Berkeley National Laboratory, Berkeley, California, 94720, United States

[∥] Department of Materials Science and Engineering, University of California at Berkeley, Berkeley, California 94720, United States

[⊥] Advanced Light Source, Lawrence Berkeley National Laboratory, Berkeley, California, 94720, United States

KEYWORDS: SNOM, graphene, solid-liquid interface, electrical double layer, near-field, nano-FTIR

ABSTRACT

We present a new methodology that enables studies of the molecular structure of graphene-liquid interfaces with nanoscale spatial resolution. It is based on Fourier transform infrared nanospectroscopy (nano-FTIR), where the infrared (IR) field is plasmonically enhanced near the tip apex of an atomic force microscope (AFM). The graphene seals a liquid electrolyte reservoir while acting also as a working electrode. The photon transparency of graphene enables IR spectroscopy studies of its interface with liquids, including water, propylene carbonate, and aqueous ammonium sulfate electrolyte solutions. We illustrate the method by comparing IR spectra obtained by nano-FTIR and attenuated total reflection (which has a detection depth of a few microns) demonstrating that the nano-FTIR method makes possible to determine changes in speciation and ion concentration in the electric double and diffuse layers as a function of bias.

TEXT

The interface between solid and liquid phases plays a fundamental role in natural and engineered materials. In biological systems, transport of molecules and transmission of signals in and out of cell membranes take place at membrane-aqueous solution interfaces[1]. In geochemical systems, interactions between solid materials and aqueous solutions are responsible for chemical weathering and soil formation[2]. In electrochemical systems, reactions such as CO_2 reduction, H_2O splitting, and corrosion phenomena occur also at the solid-liquid interface[3]. Numerous theories and models have been developed to describe the structure of solid-liquid interfaces, for example, the electrical double layer (EDL) described by Helmholtz, and the more diffuse Gouy-Chapman and Stern layers[3]. These continuum models, and modern atomistic models of solvation and interface structure through first principles density function theory (DFT) calculations, necessitate validation with experimental molecular level spectroscopy and microscopy techniques for a fundamental understanding of solid-liquid interface structure and the processes occurring there, such as charge transfer, adsorption, etc., and to improve many technologies[4].

Several new experimental methods have been recently developed that enable studies at ambient conditions. One approach uses partially immersed electrodes covered with nanometer thin electrolyte films[5, 6] to facilitate X-ray photoelectron spectroscopy (XPS) of electrode-liquid interfaces. Other methods use thin membranes, such as silicon nitride and graphene, that permit

high energy electrons and photons to penetrate, yet are strong enough to withstand pressure gradients between vacuum and liquid. These membranes have been used in transmission electron microscopy (TEM)[7-9], scanning electron microscopy (SEM)[8, 10], XPS[11-15], and X-ray absorption spectroscopy (XAS)[12, 16, 17]. Here, we utilize graphene membranes to enable nanoscale vibrational spectroscopy of graphene-electrolyte interfaces.

In contrast with X-ray or electron-based techniques, infrared (IR) spectroscopy is typically non-destructive[18], and compatible with liquid environments. For example, Fourier transform IR spectroscopy operated in the attenuated total reflectance mode (ATR-FTIR) has been used for the characterization of solid-liquid interfaces[19-21]. However, a substantial contribution of ATR-FTIR spectra originates from the bulk liquid due to the penetration depth of IR photons, ranging from hundreds of nm to micrometers[18]. Therefore, without polarization dependent selection rules that might distinguish the interface from the bulk[22, 23], such techniques can be insensitive to details within ~10 nm of the solid surface, which are the most relevant to the interfacial chemistry within the EDL and diffuse layers. Furthermore, the lateral spatial resolution is diffraction-limited by the long wavelengths of IR light, which is several micrometers.

The development of IR scattering-scanning near-field optical microscopy (s-SNOM) has overcome the diffraction limit of conventional optics to provide spatially resolved IR images down to ~10 nm. This is accomplished by illuminating the metallized tip of an atomic force microscope (AFM) with IR radiation, which produces a strong plasmonic enhancement of the electromagnetic field near its apex. The scattered light from the near-field interaction between the tip and sample is then measured[24-26]. If the illuminating IR source used is broadband, such as synchrotron radiation or super continuum lasers, Fourier transform IR nanospectroscopy (nano-FTIR) can be achieved[27, 28].

Researchers have successfully demonstrated the unique advantages of s-SNOM on numerous solid systems, for example in the nanoscale characterization of graphene plasmons[29-31], conductivity[32, 33], phase transitions[34-36], ex-situ electrochemical interfaces[37, 38], catalytic activity[39], structure of bio-materials[40, 41], polymers[24, 27], and more. Even three-dimensional tomographic reconstructions of solid electrochemical materials have been accomplished with s-SNOM approaches[42], however nanoscale IR characterization of liquid films and surfaces with s-SNOM

has proven to be very challenging. Application of s-SNOM to liquid systems have been stymied not only because of the strong absorption of IR light by the liquid, but also by the strong damping of the oscillatory motion of the AFM cantilever in close proximity with the liquid[43]. Khatib *et al.* recently demonstrated a route around this challenge by encapsulating small amounts of water and biomolecules with graphene, which provides an impermeable liquid barrier transparent to the IR light[44]. This method, however, is limited to studies involving very small liquid volumes trapped under graphene, which makes the application of bias for in-situ/operando studies difficult.

Experimental method

Figure 1(a) shows a 3D cross-sectional schematic of our graphene-based liquid cell for nano-FTIR studies under bias control. The body of the cell is made of polyether ether ketone (PEEK), an insulating solid material well-suited for machining. The liquid reservoir has a volume of several microliters and is sealed by a graphene membrane mounted on top of a perforated silicon nitride (Si_3N_4) chip with holes of 500 nm to 1 micron diameter. The chip was coated with gold (~20 nm) to improve graphene adhesion and to ensure electrical connectivity to all regions of the graphene membrane (see Supporting Information)[45]. An AFM topographic image of the graphene-capped array of holes is shown in Figure 1(b). Raman spectroscopy, Figure 1(c), from the graphene shows sharp peaks characteristic of monolayer thickness[46]. Figure 1(d) shows a schematic view of one hole to illustrate the principle of the nano-FTIR measurement through the suspended graphene separating the liquid in the cell from the ambient gas side outside.

We use the bright, spatially coherent broadband IR radiation from the Advanced Light Source (ALS), the Lawrence Berkeley National Laboratory synchrotron facility. The broadband IR is focused on the Pt-coated AFM tip on a cantilever driven to oscillate at its fundamental resonant frequency[28]. The scattered near-field signal is demodulated at the second (and higher) harmonics of the cantilever oscillation to eliminate the far field non-local scattered background (see Supporting Information)[28, 47]. Reference IR spectra are obtained with the tip over graphene on gold regions away from the holes.

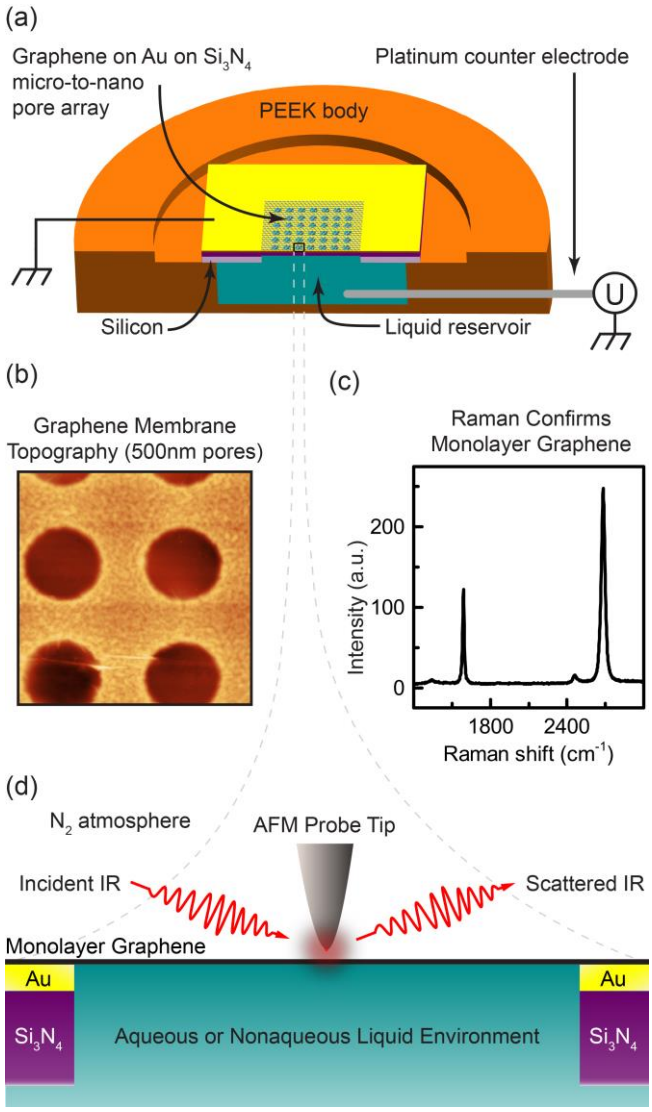

Figure 1. (a) Schematic of our graphene-capped liquid cell design with a cross-sectional view. A cavity in the body center is the liquid electrolyte reservoir. A Pt counter electrode is fed through the cell wall. The cell is sealed by a Si chip covered with a 50 nm thick perforated silicon nitride (Si_3N_4) membrane, coated with gold (~ 20 nm) and capped with graphene. The holes have diameters ranging from hundreds of nm to μm. (b) AFM image showing a region of a graphene-covered hole array (500 nm diameter). (c) Raman spectrum of graphene shows the characteristic peaks of monolayer graphene. (d) Schematic of a single graphene-capped hole with a tip apex on top, showing the incident and scattered IR beams.

Results

a) Graphene – Water Interface

Figure 2(a) shows an image of the near-field IR amplitude A_2, from the scattered light at the second harmonic of the cantilever oscillation. The imaged region includes a hole with suspended graphene covering the water-filled cell. The scattered amplitude over the suspended graphene (dark color) is much smaller than that over the gold region (gold color). This is expected from the metallic nature of the graphene-gold region, with negligible absorption of the light[24, 47], compared to the poorly reflective graphene-water region.

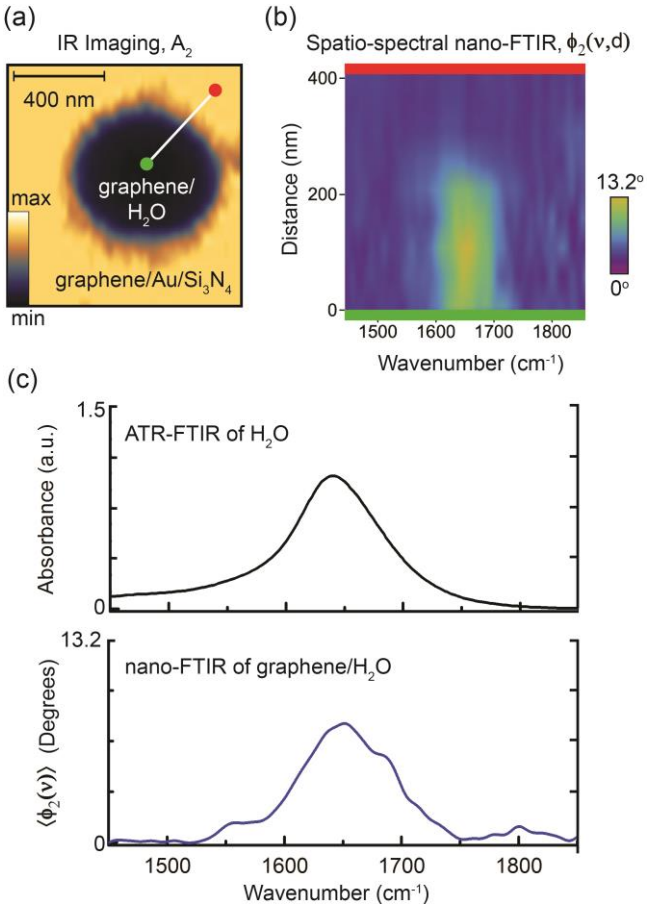

Figure 2. (a) Scattered IR amplitude image in a region containing a single hole with suspended graphene in contact with water in the cell. The IR signal is the near-field amplitude A_2, at the second harmonic of the cantilever oscillation frequency. The large contrast difference between graphene/Au/Si_3N_4 and graphene-H_2O interfaces is due to their very different dielectric and absorption properties. (b) Color map representation of nano-FTIR spectra in the water bending mode (scissor mode) region, acquired at 50 nm intervals along the white line between the red and green end points in (a). The spectra displayed here is the phase φ_2 of the scattered signal at the 2nd harmonic of the cantilever oscillation frequency, which

corresponds to the absorption coefficient of the material[26-28]. As can be seen the water bending mode peak vanishes when the AFM tip is located over graphene/Au/Si_3N_4. (c) Comparison of an ATR-FTIR measurement of a liquid droplet of H_2O (top) with nano-FTIR measurements over graphene-H_2O (bottom).

The peak from the water bending mode is clearly visible when the AFM tip is over the graphene-water interface but vanishes when the AFM tip is over the graphene-gold region, as seen in the spatially resolved nano-FTIR map, Figure 2(b). The averaged nano-FTIR spectrum on the graphene-water region is plotted on Figure 2(c) (bottom) in blue. The spectrum is overall similar to the ATR-FTIR spectrum of a droplet of the same water solution shown at the top of Figure 2(c), except for a slight blue shift. Since the plasmonic enhancement of the IR around the AFM tip decays exponentially with distance, with a decay length of the order of the tip radius[48], the nano-FTIR spectrum should be sensitive to the layers of water within the decay length, which includes the EDL and diffuse layers, with larger contribution from the first due to the exponential decay. In contrast, the ATR-FTIR probes much deeper into the solution, of the order of the infrared wavelength, i.e, several micrometers, and should thus represent the bulk of water. Although the shoulders in the nano-FTIR peak might indicate the presence of several H-bonding configurations, the current signal-to-noise ratio is not sufficient to support unambiguous assignments at this time. In addition, the hydrogen bond stretching region of water, above 3000 cm^{-1}, which is very sensitive to different bonding configurations, is unfortunately very noisy in our current set up (see Supporting Information).

b) Graphene – Non-aqueous Organic Electrolyte Interface

A second experiment was conducted using anhydrous propylene carbonate (PC), a non-aqueous organic solvent with high dipole moment used in battery electrolytes[4]. Figure 3(a) shows a broadband IR image of a graphene membrane, with PC wetting below, and the surrounding graphene/gold/Si_3N_4 region. As before the IR image is the amplitude of the second harmonic of the near-field scattered light, A_2, and the strong contrast reveals the very different dielectric properties of the two regions.

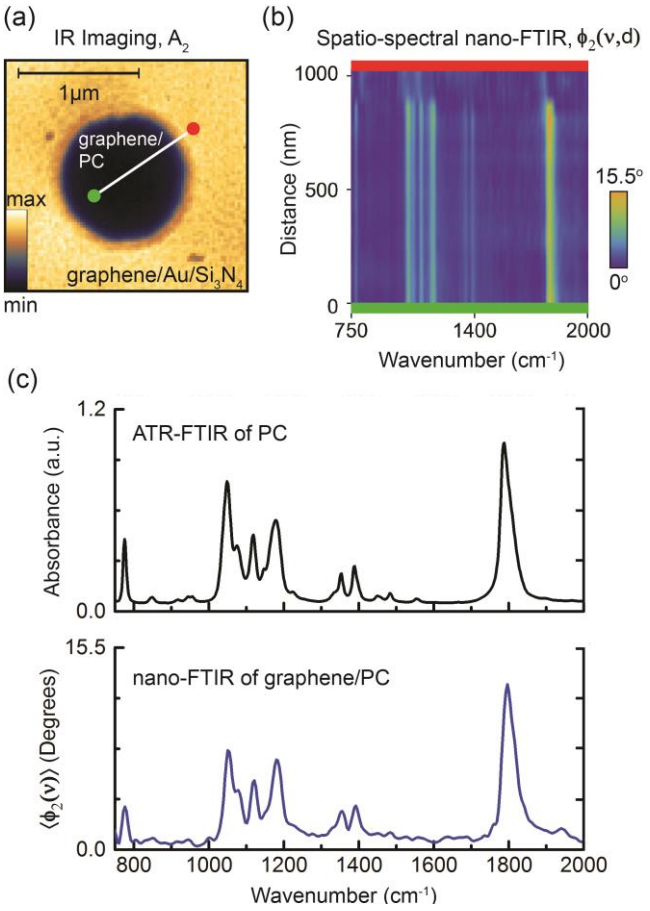

Figure 3. (a) Scattered IR amplitude image in a region containing a single hole with suspended graphene in contact with the propylene carbonate (PC) liquid in the cell. As in the previous figure the IR signal is the near-field amplitude A_2, of the second harmonic of the cantilever oscillation frequency. The white line marks the positions where nano-FTIR measurements were recorded. (b) Color map representation of the nano-FTIR measurements acquired at 50 nm step intervals over ca. 1000nm between the red and green bounding lines color-matched to points in (a). The spectra correspond to the phase φ_2 of the scattered signal at the 2nd harmonic of the cantilever oscillation frequency, which corresponds to the absorption coefficient of the material. Spectral features vanish when the AFM tip is located over graphene/Au/Si_3N_4. (c) ATR-FTIR measurement of a liquid droplet of PC (top) and nano-FTIR measurements over graphene-PC (bottom).

Nano-FTIR spectra were collected in a similar way to the water measurements along a 1,000 nm long line (white line in Figure 3(a)), and are displayed as a color map in Figure 3(b). Several bands with different peak heights can be seen only in the region where PC is in contact with the graphene membrane. These bands match well to those of PC published in the literature[49]. The

spectrum at the bottom of Figure 3(c) is the nano-FTIR measurement collected at the graphene-PC interface, which can be compared with ATR-FTIR data from a PC droplet, plotted in black on the top. Overall, the nano-FTIR and the ATR-FTIR results are very similar, with only slight differences in peak positions and heights. The similarity of two spectra indicates that the liquid structure extends nearly unchanged from bulk to interface.

c) Graphene – Ionic Salt Solution Interface

The full power of this liquid nano-FTIR method is best demonstrated in the case of electrolytes containing cations and anions that can be identified by their different vibrational characteristics. For this purpose, we chose a 0.1 M $(NH_4)_2SO_4$ aqueous solution, with the aim to identify the nature of the species formed in the EDL, likely including NH_4^+, solvated SO_4^{2-}, H_2O, etc. The cell in this experiment is similar to that in the previous two examples. We first performed ATR-FTIR on this electrolyte for three different concentrations (0.1, 1.0 and 2.0 M) to establish its characteristic IR absorption features. The result is plotted on the top panel of Figure 4(a). The expected peaks from antisymmetric S=O stretching in SO_4^{2-} and the bending modes of NH_4^+ and water can be easily detected[50]. The nano-FTIR performed over graphene covering the 0.1M electrolyte solution is shown on the bottom panel of Figure 4(a) for a potential difference of zero volts between the graphene working and Pt counter electrodes.

In contrast to the case of pure water and PC discussed above, in the 0.1 M case, very clear differences exist between ATR-FTIR and nano-FTIR spectra (black and blue curves respectively in Figure 4(a)). In the plotted wavenumber range, the ATR-FTIR measures a higher peak for water bending mode than for sulfate and ammonia. This is a result of the low relative number of solutes in the solution bulk: one (two) sulfate (ammonium) per ~ 550 water molecules at 0.1 M concentration. However, in nano-FTIR, the sulfate (ammonium) peak is larger than (similar to) the water bending mode. Moreover, additional peaks near 1200 cm^{-1} and 1300 cm^{-1} are recorded.

In order to clarify the results we need to take into account several important factors. First, the absorption cross section of the corresponding fundamental transitions are different by one-to-two orders of magnitude[51], as clearly observed in the concentration-dependent ATR-FTIR spectra on the top panel of Figure 4(a). From the spectra, we calculate that the absorption cross section for the sulfate and ammonium peaks are about 60 and 10 times, respectively, that of the water bending

peak (normalized to their molar concentrations). Second, the polarization of the field near the tip is perpendicular to the interface, which makes the nano-FTIR technique particularly sensitive to vibrational modes with transition dipole moments perpendicular to the surface[52]. Because water molecules in the interfacial layer are mostly oriented parallel to the graphene[53-55], this orientation makes the sensitivity to the bending mode of water particularly weak. Third, the depth sensitivity of each technique is very different as previously mentioned. While ATR-FTIR measures bulk structure, nano-FTIR's spatial sensitivity is constrained by the highly non-linear decay of the electric near-field with a nanoscale decay length related to tip radius of curvature[48]. In our case, this likely results in nano-FTIR spectra that are mostly dominated by IR features of species in the EDL and diffuse layer regions, rather than the bulk solution. Fourth, and lastly, is the possibility of graphene-based plasmonic enhancement[56, 57]. Although there is no apparent wavelength-dependent enhancement in the 700-2000 cm^{-1} region, as indicated by the close agreement between the ATR-FTIR and nano-FTIR relative peak heights of PC in Figure 3(c), we cannot exclude the possibility of a wavelength-dependent enhancement in the salt solution because adsorption of sulfate or ammonium species to graphene could alter the graphene doping and shift the plasmon frequency. A combination of these factors contribute to the drastically different relative peak heights observed in nano-FTIR versus ATR-FTIR, as well as the observation of interface specific peaks with nano-FTIR.

Quantification of the relative species populations within the EDL and diffuse layer requires a careful theoretical study of the electroptical activity of interfacial water and major solution components (sulfates and ammonium) under the nano-FTIR measurement conditions. By parsing the contributions of various species at different locations to the dielectric function[58, 59], we will be able to identify possible interface specific species. For example, the peaks near 1200 cm^{-1} and 1300 cm^{-1} could be assigned to interfacial ionic species formed in the solution (e.g. bisulfate ions[60]) or relatively enhanced combinational modes of solvated sulfate ions with librational modes of water. However, to better interpret the nano-FTIR spectra, a thorough thermodynamically-based analysis of all the electrolyte component's spatial distributions needs to be performed. This will require multiscale modeling of the interface, including both advanced continuum models[61] and ab initio molecular dynamics. The demonstrated capability of our method to obtain spectroscopic data from species within the EDL and diffuse layer opens a significant opportunity for future simulation work to completely identify the composition of such double and diffuse layers.

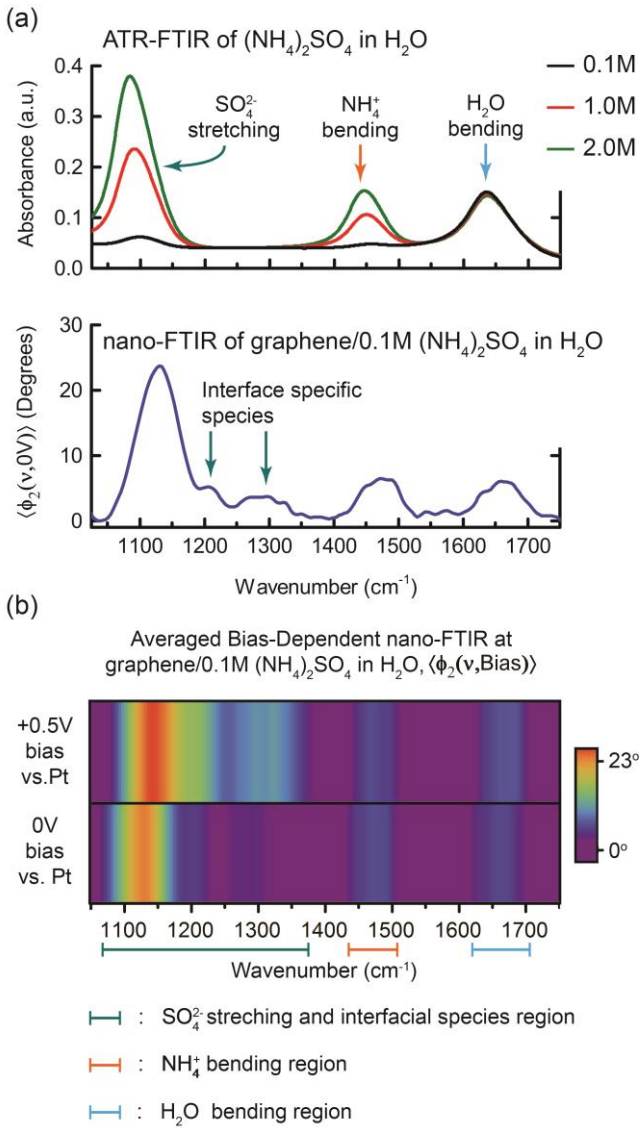

Figure 4. (a) ATR-FTIR spectra from a drop of 0.1M (black), 1M (red) and 2M (green) $(NH_4)_2SO_4$ aqueous solution (top), and nano-FTIR (bottom) of the 0.1M $(NH_4)_2SO_4$ aqueous solution at zero applied bias acquired over the suspended graphene covering the solution in the cell of Figure 1. In both cases the spectral region, between 1050 and 1750 cm^{-1}, covers the area of SO_4^{2-} stretching modes, as well as the bending modes of NH_4^+ and H_2O. Additional peaks near 1200 cm^{-1} and 1300 cm^{-1} in nano-FTIR spectrum appear from yet unidentified interfacial species. As in the previous examples the nano-FTIR appear slightly blue shifted (by ~20 cm^{-1}). (b) Bias dependent nano-FTIR displayed as a color map for +0.5V (top) and 0V bias voltages (bottom) vs the Pt counter electrode. The 0V data is an average of a total of 64 spectra collected in two separate measurements at two different points of the graphene-solution interface. The +0.5V data is an average of 112 spectra collected in 5 separate measurements at 5 different points of the graphene-solution

interface. The application of positive bias between graphene and Pt increases the relative concentration of sulfate and interfacial species near graphene, resulting in a larger measured signal.

We also studied how bias between graphene working and Pt counter electrodes affects nano-FTIR spectra. The resulting spectra are shown as color maps in Figure 4(b). The bottom spectrum was collected at a bias of 0V, while the top spectrum was collected at a bias of +0.5V relative to the Pt. A substantial change in near-field signal is observed by comparing the two data sets. At positive bias the near-field signals from the sulfate stretching, and the two interfacial species peaks increase, while ammonium and water peaks change only slightly relative to the zero bias case. The increase in the sulfate region signal upon positive graphene bias is consistent with an electrostatically induced increase in relative anion (sulfate) concentration in the EDL and diffuse layers.

In summary, we have presented the design and development of a suspended graphene liquid cell device, and methodology that enables in situ nano-FTIR with simultaneous electrostatic control of graphene-liquid interfaces. The approach was demonstrated on interfaces of graphene-water, graphene-propylene carbonate, and graphene-aqueous ammonium sulfate. The interfacial sensitivity and non-destructive nature of nano-FTIR, coupled with the use of electrically conductive graphene membranes capping a liquid cell opens new opportunities for minimally invasive, in situ and/or operando spectroscopic characterization of the graphene-electrolyte interface with full electrochemical bias control. Our electrochemical cell with fluid input/output makes possible easy refreshing and/or changing of the electrolyte. Further, this methodology of solid-liquid interface exploration is not limited to pure graphene as it can be coated with a diversity of thin inorganic or organic and living biological systems. Indeed, some of these platforms have already been tested successfully in our laboratory. This work lays the foundation for future experimental and theoretical efforts leading to a comprehensive understanding of composition and structure at a diversity of solid-liquid interfaces.

ASSOCIATED CONTENT

Supporting Information.

The Supporting Information is available free of charge on the ACS Publication website at http://pubs.acs.org.

Additional information on the graphene transfer and nano-FTIR measurements.

AUTHOR INFORMATION

Corresponding Author

*Email: mbsalmeron@lbl.gov (M.S.); R_Kostecki@lbl.gov (R.K.); habechtel@lbl.gov (H.A.B.)

Author Contributions

^These authors contributed equally to this work.

Notes

The authors declare no competing financial interest.

ACKNOWLEDGMENTS

This work was supported by the Office of Basic Energy Sciences (BES), Division of Materials Sciences and Engineering, of the U.S. Department of Energy (DOE) under Contract No. DE-AC02-05CH11231, through the Structure and Dynamics of Materials Interfaces program (FWP KC31SM). The nano-FTIR measurements were performed at BL 2.4 and 5.4 of the Advanced Light Source, supported by DOE under the same contract. Sample preparation, Raman and AFM characterization were performed at the Molecular Foundry supported by DOE under the same contract. Funding support to J.L., H.B. and R.K. was provided by the Energy & Biosciences Institute through the EBI-Shell program. We are grateful to Ed Wong of the Molecular Foundry for his assistance in fabricating the liquid cell. We are also grateful to Michael C. Martin of the Advanced Light Source for helpful suggestions.

REFERENCES

1. Krepkiy, D.; Mihailescu, M.; Freites, J. A.; Schow, E. V.; Worcester, D. L.; Gawrisch, K.; Tobias, D. J.; White, S. H.; Swartz, K. J. *Nature* **2009,** 462, (7272), 473-U168.
2. Putnis, A. *Science* **2014,** 343, (6178), 1441-1442.
3. Bard, A. J.; Faulkner, L. R., *Electrochemical methods : fundamentals and applications*. 2nd ed.; John Wiley: New York, 2000; p xxi, 833 p.
4. Gauthier, M.; Carney, T. J.; Grimaud, A.; Giordano, L.; Pour, N.; Chang, H. H.; Fenning, D. P.; Lux, S. F.; Paschos, O.; Bauer, C.; Magia, F.; Lupart, S.; Lamp, P.; Shao-Horn, Y. *J Phys Chem Lett* **2015,** 6, (22), 4653-4672.
5. Favaro, M.; Jeong, B.; Ross, P. N.; Yano, J.; Hussain, Z.; Liu, Z.; Crumlin, E. J. *Nat Commun* **2016,** 7.
6. Axnanda, S.; Crumlin, E. J.; Mao, B. H.; Rani, S.; Chang, R.; Karlsson, P. G.; Edwards, M. O. M.; Lundqvist, M.; Moberg, R.; Ross, P.; Hussain, Z.; Liu, Z. *Sci Rep-Uk* **2015,** 5.
7. Zheng, H. M.; Smith, R. K.; Jun, Y. W.; Kisielowski, C.; Dahmen, U.; Alivisatos, A. P. *Science* **2009,** 324, (5932), 1309-1312.
8. de Jonge, N.; Ross, F. M. *Nat Nanotechnol* **2011,** 6, (11), 695-704.
9. Yuk, J. M.; Park, J.; Ercius, P.; Kim, K.; Hellebusch, D. J.; Crommie, M. F.; Lee, J. Y.; Zettl, A.; Alivisatos, A. P. *Science* **2012,** 336, (6077), 61-64.
10. Yulaev, A.; Guo, H. X.; Strelcov, E.; Chen, L.; Vlassiouk, I.; Kolmakov, A. *Acs Appl Mater Inter* **2017,** 9, (31), 26492-26502.
11. Kolmakov, A.; Dikin, D. A.; Cote, L. J.; Huang, J. X.; Abyaneh, M. K.; Amati, M.; Gregoratti, L.; Gunther, S.; Kiskinova, M. *Nat Nanotechnol* **2011,** 6, (10), 651-657.
12. Wu, C. H.; Weatherup, R. S.; Salmeron, M. B. *Phys Chem Chem Phys* **2015,** 17, (45), 30229-30239.
13. Velasco-Velez, J. J.; Pfeifer, V.; Havecker, M.; Weatherup, R. S.; Arrigo, R.; Chuang, C. H.; Stotz, E.; Weinberg, G.; Salmeron, M.; Schlogl, R.; Knop-Gericke, A. *Angew Chem Int Edit* **2015,** 54, (48), 14554-14558.
14. Guo, H. X.; Strelcov, E.; Yulaev, A.; Wang, J.; Appathurai, N.; Urquhart, S.; Vinson, J.; Sahu, S.; Zwolak, M.; Kolmakov, A. *Nano Lett* **2017,** 17, (2), 1034-1041.
15. Nemsak, S.; Strelcov, E.; Duchon, T.; Guo, H. X.; Hackl, J.; Yulaev, A.; Vlassiouk, I.; Mueller, D. N.; Schneider, C. M.; Kolmakov, A. *J Am Chem Soc* **2017,** 139, (50), 18138-18141.
16. Velasco-Velez, J. J.; Wu, C. H.; Pascal, T. A.; Wan, L. W. F.; Guo, J. H.; Prendergast, D.; Salmeron, M. *Science* **2014,** 346, (6211), 831-834.
17. Wu, C. H.; Pascal, T. A.; Baskin, A.; Wang, H. X.; Fang, H. T.; Liu, Y. S.; Lu, Y. H.; Guo, J. H.; Prendergast, D.; Salmeron, M. B. *J Am Chem Soc* **2018,** 140, (47), 16237-16244.
18. Zaera, F. *Chem Rev* **2012,** 112, (5), 2920-2986.
19. Hind, A. R.; Bhargava, S. K.; McKinnon, A. *Adv Colloid Interfac* **2001,** 93, (1-3), 91-114.
20. McQuillan, A. J. *Adv Mater* **2001,** 13, (12-13), 1034-+.
21. Andanson, J. M.; Baiker, A. *Chem Soc Rev* **2010,** 39, (12), 4571-4584.
22. Herlihy, D. M.; Waegele, M. M.; Chen, X. H.; Pemmaraju, C. D.; Prendergast, D.; Cuk, T. *Nat Chem* **2016,** 8, (6), 556-556.
23. Chen, X. H.; Choing, S. N.; Aschaffenburg, D. J.; Pemmaraju, C. D.; Prendergast, D.; Cuk, T. *J Am Chem Soc* **2017,** 139, (5), 1830-1841.

24. Knoll, B.; Keilmann, F. *Nature* **1999,** 399, (6732), 134-137.
25. Atkin, J. M.; Berweger, S.; Jones, A. C.; Raschke, M. B. *Adv Phys* **2012,** 61, (6), 745-842.
26. Centrone, A. *Annu Rev Anal Chem* **2015,** 8, 101-126.
27. Huth, F.; Govyadinov, A.; Amarie, S.; Nuansing, W.; Keilmann, F.; Hilenbrand, R. *Nano Lett* **2012,** 12, (8), 3973-3978.
28. Bechtel, H. A.; Muller, E. A.; Olmon, R. L.; Martin, M. C.; Raschke, M. B. *P Natl Acad Sci USA* **2014,** 111, (20), 7191-7196.
29. Gerber, J. A.; Berweger, S.; O'Callahan, B. T.; Raschke, M. B. *Phys Rev Lett* **2014,** 113, (5).
30. Chen, J. N.; Badioli, M.; Alonso-Gonzalez, P.; Thongrattanasiri, S.; Huth, F.; Osmond, J.; Spasenovic, M.; Centeno, A.; Pesquera, A.; Godignon, P.; Elorza, A. Z.; Camara, N.; de Abajo, F. J. G.; Hillenbrand, R.; Koppens, F. H. L. *Nature* **2012,** 487, (7405), 77-81.
31. Fei, Z.; Rodin, A. S.; Andreev, G. O.; Bao, W.; McLeod, A. S.; Wagner, M.; Zhang, L. M.; Zhao, Z.; Thiemens, M.; Dominguez, G.; Fogler, M. M.; Castro Neto, A. H.; Lau, C. N.; Keilmann, F.; Basov, D. N. *Nature* **2012,** 487, (7405), 82-85.
32. Huber, A. J.; Kazantsev, D.; Keilmann, F.; Wittborn, J.; Hillenbrand, R. *Adv Mater* **2007,** 19, (17), 2209-+.
33. Stiegler, J. M.; Huber, A. J.; Diedenhofen, S. L.; Rivas, J. G.; Algra, R. E.; Bakkers, E. P. A. M.; Hillenbrand, R. *Nano Lett* **2010,** 10, (4), 1387-1392.
34. Liu, M. K.; Sternbach, A. J.; Wagner, M.; Slusar, T. V.; Kong, T.; Bud'ko, S. L.; Kittiwatanakul, S.; Qazilbash, M. M.; McLeod, A.; Fei, Z.; Abreu, E.; Zhang, J. D.; Goldflam, M.; Dai, S. Y.; Ni, G. X.; Lu, J. W.; Bechtel, H. A.; Martin, M. C.; Raschke, M. B.; Averitt, R. D.; Wolf, S. A.; Kim, H. T.; Canfield, P. C.; Basov, D. N. *Phys Rev B* **2015,** 91, (24).
35. Qazilbash, M. M.; Brehm, M.; Chae, B. G.; Ho, P. C.; Andreev, G. O.; Kim, B. J.; Yun, S. J.; Balatsky, A. V.; Maple, M. B.; Keilmann, F.; Kim, H. T.; Basov, D. N. *Science* **2007,** 318, (5857), 1750-1753.
36. McLeod, A. S.; van Heumen, E.; Ramirez, J. G.; Wang, S.; Saerbeck, T.; Guenon, S.; Goldflam, M.; Anderegg, L.; Kelly, P.; Mueller, A.; Liu, M. K.; Schuller, I. K.; Basov, D. N. *Nat Phys* **2017,** 13, (1), 80-86.
37. Ayache, M.; Jong, D.; Syzdek, J.; Kostecki, R. *J Electrochem Soc* **2015,** 162, (13), A7078-A7082.
38. Ayache, M.; Lux, S. F.; Kostecki, R. *J Phys Chem Lett* **2015,** 6, (7), 1126-1129.
39. Wu, C. Y.; Wolf, W. J.; Levartovsky, Y.; Bechtel, H. A.; Martin, M. C.; Toste, F. D.; Gross, E. *Nature* **2017,** 541, (7638), 511-515.
40. Brehm, M.; Taubner, T.; Hillenbrand, R.; Keilmann, F. *Nano Lett* **2006,** 6, (7), 1307-1310.
41. Amenabar, I.; Poly, S.; Nuansing, W.; Hubrich, E. H.; Govyadinov, A. A.; Huth, F.; Krutokhvostov, R.; Zhang, L. B.; Knez, M.; Heberle, J.; Bittner, A. M.; Hillenbrand, R. *Nat Commun* **2013,** 4.
42. Lucas, I. T.; McLeod, A. S.; Syzdek, J. S.; Middlemiss, D. S.; Grey, C. P.; Basov, D. N.; Kostecki, R. *Nano Lett* **2015,** 15, (1), 1-7.
43. Jin, M. Z.; Lu, F.; Belkin, M. A. *Light-Sci Appl* **2017,** 6.
44. Khatib, O.; Wood, J. D.; McLeod, A. S.; Goldflam, M. D.; Wagner, M.; Damhorst, G. L.; Koepke, J. C.; Doidge, G. P.; Rangarajan, A.; Bashir, R.; Pop, E.; Lyding, J. W.; Thiemens, M. H.; Keilmann, F.; Basov, D. N. *Acs Nano* **2015,** 9, (8), 7968-7975.

45. Weatherup, R. S.; Eren, B.; Hao, Y. B.; Bluhm, H.; Salmeron, M. B. *J Phys Chem Lett* **2016,** 7, (9), 1622-1627.
46. Ferrari, A. C.; Meyer, J. C.; Scardaci, V.; Casiraghi, C.; Lazzeri, M.; Mauri, F.; Piscanec, S.; Jiang, D.; Novoselov, K. S.; Roth, S.; Geim, A. K. *Phys Rev Lett* **2006,** 97, (18).
47. Keilmann, F.; Hillenbrand, R. *Philos T R Soc A* **2004,** 362, (1817), 787-805.
48. Huber, A. J.; Keilmann, F.; Wittborn, J.; Aizpurua, J.; Hillenbrand, R. *Nano Lett* **2008,** 8, (11), 3766-3770.
49. Brooksby, P. A.; Fawcett, W. R. *Spectrochim Acta A* **2006,** 64, (2), 372-382.
50. Kadam, S. S.; Mesbah, A.; van der Windt, E.; Kramer, H. J. M. *Chem Eng Res Des* **2011,** 89, (7a), 995-1005.
51. Zhou, J.; Santambrogio, G.; Brummer, M.; Moore, D. T.; Meijer, G.; Neumark, D. M.; Asmis, K. R. *J Chem Phys* **2006,** 125, (11).
52. Muller, E. A.; Pollard, B.; Bechtel, H. A.; van Blerkom, P.; Raschke, M. B. *Sci Adv* **2016,** 2, (10), e1601006.
53. Don, V. S.; David, R.; Du, P.; Milet, A.; Kumar, R. *J Phys Chem B* **2019,** 123, (7), 1636-1649.
54. Maekawa, Y.; Sasaoka, K.; Yamamoto, T. *Jpn J Appl Phys* **2018,** 57, (3).
55. Singla, S.; Anim-Danso, E.; Islam, A. E.; Ngo, Y.; Kim, S. S.; Naik, R. R.; Dhinojwala, A. *Acs Nano* **2017,** 11, (5), 4899-4906.
56. de Abajo, F. J. G. *Acs Photonics* **2014,** 1, (3), 135-152.
57. Li, P. N.; Wang, T.; Bockmann, H.; Taubner, T. *Nano Lett* **2014,** 14, (8), 4400-4405.
58. Sharma, M.; Wu, Y. D.; Car, R. *Int J Quantum Chem* **2003,** 95, (6), 821-829.
59. Wang, C. C.; Tan, J. Y.; Liu, L. H. *Aip Adv* **2017,** 7, (3).
60. Yacovitch, T. I.; Wende, T.; Jiang, L.; Heine, N.; Meijer, G.; Neumark, D. M.; Asmis, K. R. *J Phys Chem Lett* **2011,** 2, (17), 2135-2140.
61. Baskin, A.; Prendergast, D. *J Chem Phys* **2019,** 150, (4).